ADVANCED SCIENCE Open Access
www.advancedscience.com

Polarity-Reversal of Exchange Bias in van der Waals $FePS_3/Fe_3GaTe_2$ Heterostructures

Han Xiao, Bingbing Lyu, Mengjuan Mi, Jian Yuan, Xiandong Zhang, Lixuan Yu, Qihui Cui, Chaofan Wang, Jun Song, Mingyuan Huang, Yufeng Tian, Liang Liu, Takashi Taniguchi, Kenji Watanabe, Min Liu, Yanfeng Guo,* Shanpeng Wang,* and Yilin Wang**

Exchange bias (EB) in antiferromagnetic (AFM)/ferromagnetic heterostructures is crucial for the advancement of spintronic devices and has attracted significant attention. The common EB effect in van der Waals heterostructures features a low blocking temperature (T_b) and a single polarity. In this work, a significant EB effect with a T_b up to 150 K is observed in $FePS_3/Fe_3GaTe_2$ heterostructures, and in particular, the EB exhibits an unusual temperature-dependent polarity-reversal behavior. Under a high positive field-cooling condition (e.g., $\mu_0 H \geq 0.5$ T), a negative EB field (H_{EB}) is observed at low temperatures, and with increasing temperature, the H_{EB} crosses zero at ≈20 K, subsequently becomes positive and later approaches zero again at T_b. A model composed of a top $FePS_3$/interfacial $FePS_3/Fe_3GaTe_2$ sandwich structure is proposed. The charge transfer from Fe_3GaTe_2 to $FePS_3$ at the interface induces net magnetic moments (ΔM) in $FePS_3$. The interface favors AFM coupling, and thus the reversal of ΔM of the interfacial $FePS_3$ leads to the polarity-reversal of EB. Moreover, the EB can be extended to the bare Fe_3GaTe_2 region of the Fe_3GaTe_2 flake partially covered by $FePS_3$. This work provides opportunities for a deeper understanding of the EB effect and opens a new route toward constructing novel spintronic devices.

1. Introduction

The magnetic proximity effect, originating from the interfacial coupling of heterostructures, facilitates a plurality of intriguing physical phenomena, including skyrmions,[1,2] magnons,[3,4] exchange bias (EB),[5] etc., and has garnered considerable attention. EB arises from the exchange coupling between a ferromagnetic (FM) layer and an antiferromagnetic (AFM) layer,[6,7] which causes the spins of the FM layer to be pinned by the AFM layer,[8] or applies a torque to the AFM layer.[9,10] The properties of AFM and FM materials, including crystal structure, magnetic anisotropy, magnetic domains, as well as interface quality, have a significant impact on the EB effect.[5,11] Achieving a high-quality interface with 3D materials is challenging due to lattice mismatch and atomic diffusion during the epitaxial growth process.[12] Van der Waals (vdW) magnets facilitate to form

H. Xiao, B. Lyu, M. Mi, L. Yu, M. Liu, Y. Wang
School of Integrated Circuits
Shandong Technology Center of Nanodevices and Integration
State Key Laboratory of Crystal Materials
Shandong University
Jinan 250100, China
E-mail: liumin@sdu.edu.cn; yilinwang@email.sdu.edu.cn

J. Yuan, Y. Guo
School of Physical Science and Technology
ShanghaiTech University
Shanghai 201210, China
E-mail: guoyf@shanghaitech.edu.cn

X. Zhang, J. Song
Shandong Wanbo Technologies Co. LTD
Jinan 250100, China

Q. Cui, S. Wang
State Key Laboratory of Crystal Materials
Institute of Crystal Materials
Shandong University
Jinan 250100, China
E-mail: wshp@sdu.edu.cn

C. Wang, M. Huang
Department of Physics
Southern University of Science and Technology
Shenzhen 518055, China

Y. Tian, L. Liu
School of Physics
Shandong University
Jinan 250100, China

T. Taniguchi
Research Center for Materials Nanoarchitectonics
National Institute for Materials Science
Tsukuba 305-0044, Japan

K. Watanabe
Research Center for Electronic and Optical Materials
National Institute for Materials Science
Tsukuba 305-0044, Japan

Y. Guo
ShanghaiTech Laboratory for Topological Physics
ShanghaiTech University
Shanghai 201210, China

The ORCID identification number(s) for the author(s) of this article can be found under https://doi.org/10.1002/advs.202409210

DOI: 10.1002/advs.202409210

an atomically sharp and ultraclean interface because their surfaces are free of dangling bonds,[13–16] and thus provide a desired platform for the investigation of EB.

Significant EB has been broadly observed in various vdW AFM/FM heterostructures, e.g., $CrCl_3/Fe_3GeTe_2$,[17] $MnPX_3/Fe_3GeTe_2$ (X = S, Se),[18,19] $CrPS_4/Fe_3GeTe_2$,[20] $CrOCl/Fe_3GeTe_2$,[21] $FePS_3/Fe_5GeTe_2$,[22] $CrI_3/MnBi_2Te_4$,[23] etc. In the $FePS_3/Fe_3GeTe_2$ heterostructure, the Curie temperature (T_C) of Fe_3GeTe_2 was elevated from 150 to 180 K, and the coercive field was also enhanced by ≈100%.[24] The EB effect is dependent on the magnitude of the magnetic field during the cooling process. In the $CrPS_4/(Fe_{0.74}Co_{0.26})_3GeTe_2$ heterostructure, a negative EB was observed with a low cooling field, while the EB was suppressed or even eliminated with an increased cooling field.[20] In oxidized-$Fe_3GeTe_2/Fe_3GeTe_2/CrSe$ heterostructure, a substantially large exchange bias field (H_{EB}) of ≈90 mT was observed at low temperature, and the H_{EB} gradually diminishes in magnitude as temperature increases until reaching the blocking temperature (T_b, the temperature at which the H_{EB} becomes zero).[25] The EB effect can also be influenced by various extrinsic stimuli. For instance, in the $FePSe_3/Fe_3GeTe_2$ heterostructure, modulation of interface spacing through pressure engineering significantly enhances the H_{EB} and T_b.[11] In another example, the application of a solid protonic gate in the $FePS_3/Fe_5GeTe_2$ heterostructure toggles the presence or absence of EB by directly introducing protons into the interface.[22] The H_{EB} is sensitive to the cooling field, interface spacing, and carrier density, while the polarity of EB does not change with varying temperatures. Polarity-reversal of EB is valuable for the design of novel spintronic devices[26,27] and has been observed in certain 3D systems,[28,29] while it is scarce in vdW heterostructures.

Among the intrinsic vdW magnets, the recently discovered ferromagnet Fe_3GaTe_2 has the highest T_C (up to 380 K for bulk and 350 K for 9.5 nm nanosheet), and exhibits itinerant ferromagnetism with robust large perpendicular magnetic anisotropy, positioning it as a promising candidate for practical applications.[30–34] The Ising-type antiferromagnet $FePS_3$ features a zigzag antiferromagnetic structure and strong out-of-plane magnetic anisotropy,[35] and maintains a constant Néel temperature (T_N) of 115 K regardless of thickness from bulk to monolayer.[36] In addition, $FePS_3$ has a band gap of 2.18 eV in a thin layer and behaves as an insulator,[37] ensuring that current mainly flows through the metallic (or semiconducting) layer in the heterostructure through electrical measurements. Thus, the vdW heterostructure of $FePS_3/Fe_3GaTe_2$ is appealing for exploring the EB effect.

In this work, a significant EB was observed in $FePS_3/Fe_3GaTe_2$ heterostructures by both anomalous Hall effect (AHE) measurements and reflective magnetic circular dichroism (RMCD). Furthermore, the EB induced at the interface of the $FePS_3/Fe_3GaTe_2$ heterostructure can laterally extend to the exposed region of the same Fe_3GaTe_2 flake, and such non-local EB effect is attributed to the itinerant ferromagnetism and the single-domain state of Fe_3GaTe_2. More interestingly, the EB features an unusual polarity-reversal behavior (from negative EB to positive EB) with increasing temperature under a suitable high-field cooling condition (e.g., $\mu_0 H \geq 0.5$ T). An intuitive model consisting of top $FePS_3$/interfacial $FePS_3/Fe_3GaTe_2$ is proposed, and the reversal of the net magnetic moments of the interfacial $FePS_3$ layer is responsible for the polarity-reversal of EB.

2. Results and Discussion

2.1. Construction of $FePS_3/Fe_3GaTe_2$ Heterostructure

Thin Fe_3GaTe_2 flakes, $FePS_3$ flakes, and $FePS_3/Fe_3GaTe_2$ heterostructures were obtained by mechanical exfoliation and dry transfer techniques in a glove box, and details can be found in the experimental sections. **Figure 1a** illustrates anomalous Hall resistance (R_{xy}) of Fe_3GaTe_2 flake with a thickness of ≈18 nm at different temperatures, indicating the absence of EB in the isolated Fe_3GaTe_2 flakes. The upper and lower panels in Figure 1b show a schematic diagram and an optical image of the constructed $FePS_3/Fe_3GaTe_2$ heterostructure (Device 1), respectively, where a thin $FePS_3$ layer (5 nm) is stacked on a Fe_3GaTe_2 layer (25 nm), and the Fe_3GaTe_2 layer is in direct contact with the pre-patterned electrodes. The $FePS_3/Fe_3GaTe_2$ heterostructure was protected by covering a h-BN layer. Raman scattering techniques were employed to assess the quality of the $FePS_3/Fe_3GaTe_2$ heterostructure, as shown in Figure 1c, the Raman signatures of the heterostructure region display a superposition of the Raman peaks of individual Fe_3GaTe_2 and $FePS_3$ flakes,[24,30,36] and no additional peaks are observed.

2.2. Temperature- and H_{cool}-Dependent Polarity-Reversal of EB

The interfacial exchange interaction of $FePS_3/Fe_3GaTe_2$ heterostructure was initially investigated by AHE measurement. **Figure 2a** illustrates the typical temperature-dependent R_{xy} of Device 1 with a positive cooling field (H_{cool}) of 1 T. The H_{cool}, perpendicular to the surface of the device, was applied at 320 K, after which the device was cooled down to a preset temperature for measurements. An obvious asymmetrical hysteresis loop with respect to the zero magnetic field was observed at low temperatures, indicating the emergence of EB. H_{EB}, which characterizes the strength of EB in a system, is defined by a relation $H_{EB} = (H_C^+ + H_C^-)/2$ where H_C^+ and H_C^- represent the positive coercive field and negative coercive field, respectively.[7,20] At 2 K, the H_{EB} is negative, indicating that the polarity of EB is negative. As temperature increases, the H_{EB} crosses zero and gradually becomes positive, demonstrating that the polarity of EB reverses from negative to positive ≈20 K, and remains positive until T_b of 150 K. To establish a direct comparison, the hysteresis loops of Device 1 at 10 and 20 K are shown in Figure 2b.

When the direction of the cooling field is reversed, the sign of H_{EB} is also reversed. As shown in Figure 2c, when a negative H_{cool} of −1 T was applied, the H_{EB} was positive at 2 K, and as the temperature increased, the H_{EB} crossed zero and gradually became negative, also demonstrating the polarity-reversal behavior of EB with increasing temperature. Figure 2d compares the temperature-dependent H_{EB} with H_{cool} = 1 T and H_{cool} = −1 T. The overall trends of the temperature-dependent H_{EB} for H_{cool} = ± 1 T are nearly symmetric, and both exhibit polarity-reversal behavior of EB at ≈20 K. The amplitude of $|H_{EB}|$ exhibits a non-monotonic relationship with temperature: $|H_{EB}|$

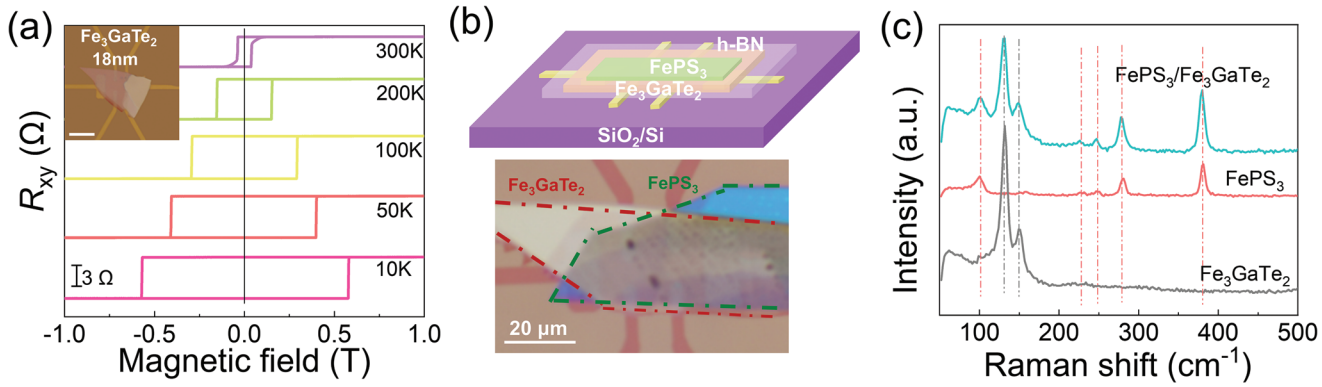

Figure 1. a) Temperature-dependent R_{xy} for isolated Fe_3GaTe_2 flake (18 nm). Inset: the optical image of the isolated Fe_3GaTe_2 device (scale bar 20 μm). b) Schematic of the vdW $FePS_3/Fe_3GaTe_2$ heterostructure covered with a h-BN layer (upper panel), and optical image of Device 1 with $FePS_3$ (5 nm)/Fe_3GaTe_2 (25 nm) heterostructure (lower panel, scale bar 20 μm). c) Raman spectra of $FePS_3/Fe_3GaTe_2$ heterostructure, individual Fe_3GaTe_2 flake, and individual $FePS_3$ flake.

initially decreases until ≈20 K, then increases to reach a maximum value at 40–60 K, and later gradually decreases until finally disappears at ≈150 K. Moreover, the slight asymmetry observed in H_{EB} under $H_{cool} = \pm 1$ T, especially at 40 K, may be attributed to the pinning effect induced by interfacial defects formed during the fabrication of the heterostructure. The pinning effect may be dependent on specific conditions, under $H_{cool} = \pm 0.5$ T, the temperature-dependent H_{EB} appears more symmetric, as shown in Figure S2 (Supporting Information). The T_b in $FePS_3/Fe_3GaTe_2$ heterostructure significantly surpasses that of $FePS_3/Fe_5GeTe_2$ (T_b ≈30 K)[22] and $FePSe_3/Fe_3GeTe_2$ (T_b ≈20 K).[11] The substantially high T_b is attributed to the strong magnetic coupling at the interface between the ultra-thin $FePS_3$ and Fe_3GaTe_2 layers, which is further demonstrated by the large $|H_{EB}|$ greater than 50 mT. Moreover, the T_b is higher than the T_N of $FePS_3$, which may arise from possible short-range spin correlation in $FePS_3$.[38]

According to the Meiklejohn–Bean model,[39] EB is also affected by the magnitude of the cooling field. The temperature-dependent R_{xy} of Device 1 under H_{cool} varied from 0.002, 0.2, 0.5, and 3 T were further investigated. As shown in **Figure 3a**, under $H_{cool} = 0.2$ T, the negative EB is observed and the

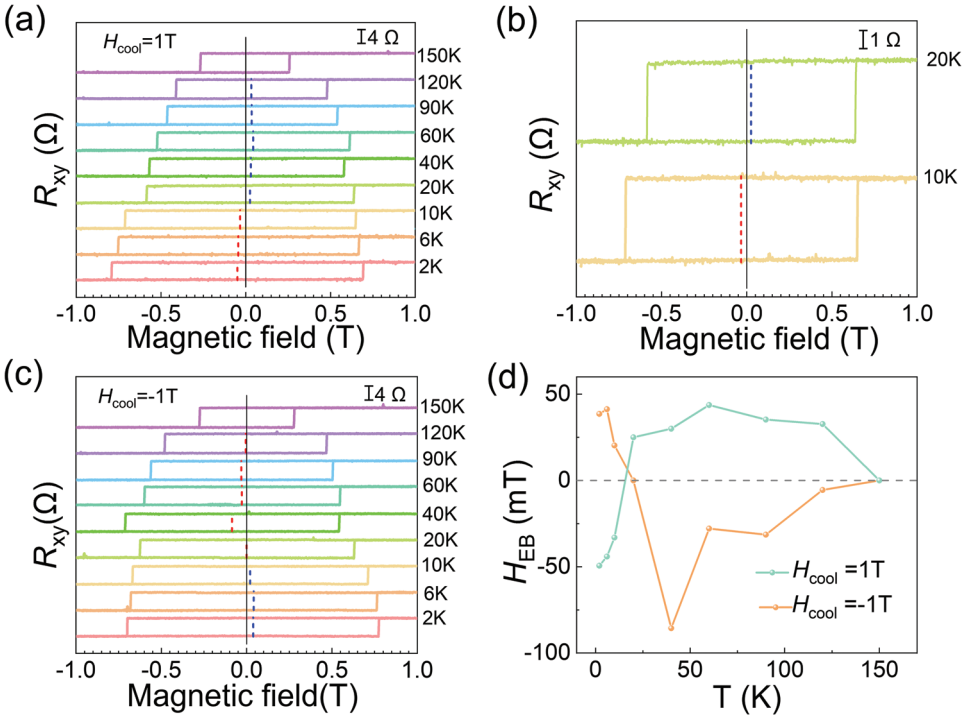

Figure 2. Significant EB effect in Device 1. a) Temperature-dependent R_{xy} under $H_{cool} = 1$ T. b) Comparison of R_{xy} at 10 and 20 K under $H_{cool} = 1$ T. c) Temperature-dependent R_{xy} under $H_{cool} = -1$ T. d) Temperature-dependent H_{EB} under $H_{cool} = \pm 1$ T.

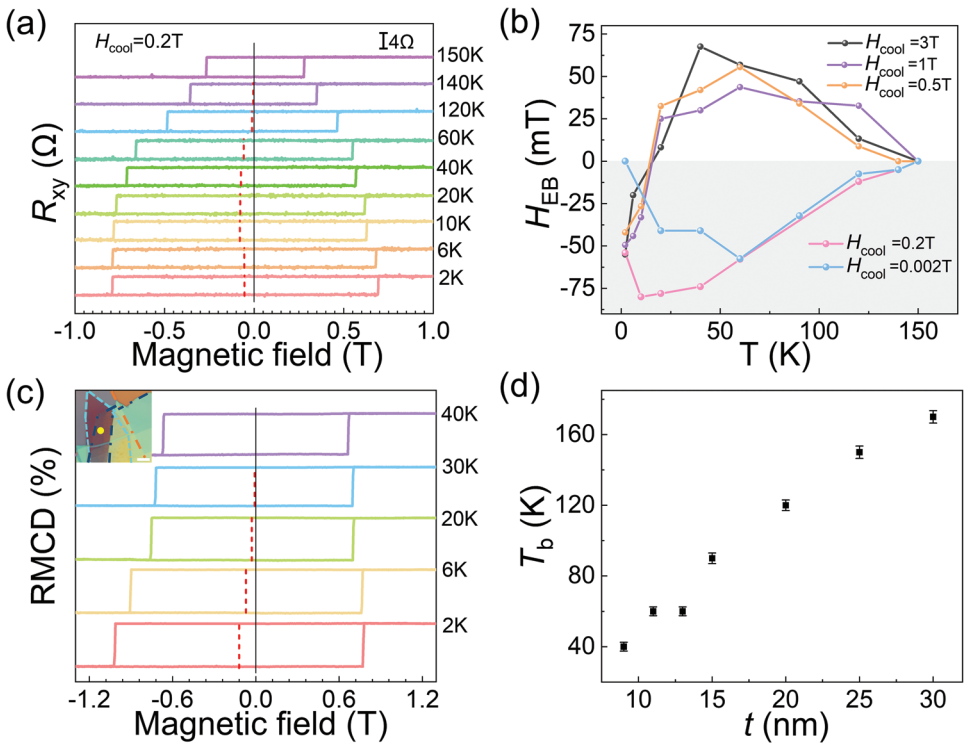

Figure 3. a) Temperature-dependent R_{xy} for Device 1 under H_{cool} = 0.2 T. b) Temperature-dependent H_{EB} for Device 1 under applied H_{cool} varied from 0.002, 0.2, 0.5, 1 and 3 T. c) Temperature-dependent RMCD hysteresis loops of $FePS_3$ (5 nm)/Fe_3GaTe_2 (9 nm). Inset: optical image of $FePS_3$/Fe_3GaTe_2 heterostructure (scale bar 10 μm). d) Thickness-dependent T_b of the $FePS_3$ (5 nm)/Fe_3GaTe_2 (t nm) heterostructures. Error bars represent deviation.

polarity remains negative until T_b of 150 K. The non-monotonic relationship between $|H_{EB}|$ and temperature is also observed, where $|H_{EB}|$ first increases and then decreases as the temperature increases. The temperature-dependent R_{xy} of Device 1 under other cooling fields is illustrated and discussed in supporting information (Figures S3, S4, Supporting Information). Figure 3b summarizes the temperature-dependent H_{EB} under different magnitudes of H_{cool}. As the temperature increases, the polarity of EB reverses from negative to positive at ≈20 K for a suitable high cooling field of $H_{cool} \geq 0.5$ T, while remaining negative for a relatively low cooling field of $H_{cool} \leq 0.2$ T, evidencing that the temperature-dependent polarity-reversal of EB requires a suitable field-cooling condition. In addition, the maximum values of $|H_{EB}|$ slightly vary depending on the magnitudes of H_{cool}, and reach a maximum $|H_{EB}|$ of 76 mT for $H_{cool} \leq 0.2$ T. The T_b is unaffected by the magnitudes of H_{cool}, and the EB effect under varying cooling fields disappears at ≈150 K. Further, as shown in Figure S5 (Supporting Information), the similar temperature-dependent polarity-reversal behavior of EB was also observed in other devices with different Fe_3GaTe_2 thickness (30, 15, 13 and 10 nm), and the temperature at which the polarity reverses decrease as the Fe_3GaTe_2 thickness decreases. Therefore, it is evident that the temperature-dependent polarity reversal of EB in $FePS_3$/Fe_3GaTe_2 heterostructures is robust and repeatable.

The EB effect in $FePS_3$/Fe_3GaTe_2 heterostructure was also observed by RMCD, which reveals the interfacial coupling at the microscopic scale.[21] The temperature-dependent RMCD hysteresis loops of isolated Fe_3GaTe_2 (10 nm) are symmetric with respect to the zero magnetic field (Figure S6, Supporting Information), revealing the absence of EB, which is also consistent with the AHE measurements. Figure 3c illustrates the temperature-dependent RMCD hysteresis loops of the $FePS_3$/Fe_3GaTe_2 (5 nm/9 nm) heterostructure, and the corresponding optical image is shown in the inset of Figure 3c. A negative EB with an absolute value $|H_{EB}|$ of 126 mT was observed at 2 K, and $|H_{EB}|$ gradually decreases as the temperature increases and becomes zero until T_b of 40 K. Moreover, because of the zero field-cooling condition for RMCD measurements, the polarity-reversal behavior of EB was not observed.

Figure 3d summarizes the variation of T_b as a function of the Fe_3GaTe_2 thickness. The T_b monotonically increases from 40 to 170 K as the FM layer thickness increases from 9 to 30 nm with the $FePS_3$ thickness fixed at 5 nm. The maximum absolute value of H_{EB} also monotonically increases from ≈38 to ≈120 mT with increasing the Fe_3GaTe_2 layer thickness, as shown in Figure S7 (Supporting Information). Such a similar relationship between the strength of EB and FM layer thickness was also observed in other heterostructures such as $CrCl_3$/Fe_3GeTe_2,[17] $CrPS_4$/$(Fe_{0.74}Co_{0.26})_3GeTe_2$ [20] and oxidized-Fe_3GeTe_2/Fe_3GeTe_2.[40] The enhancement of EB as the FM layer thickness increases is attributed to that the FM flakes with larger thickness have higher volume magnetization[17,20,40] and favor improved interface quality due to the reduction of surface roughness of the FM layer.[41,42]

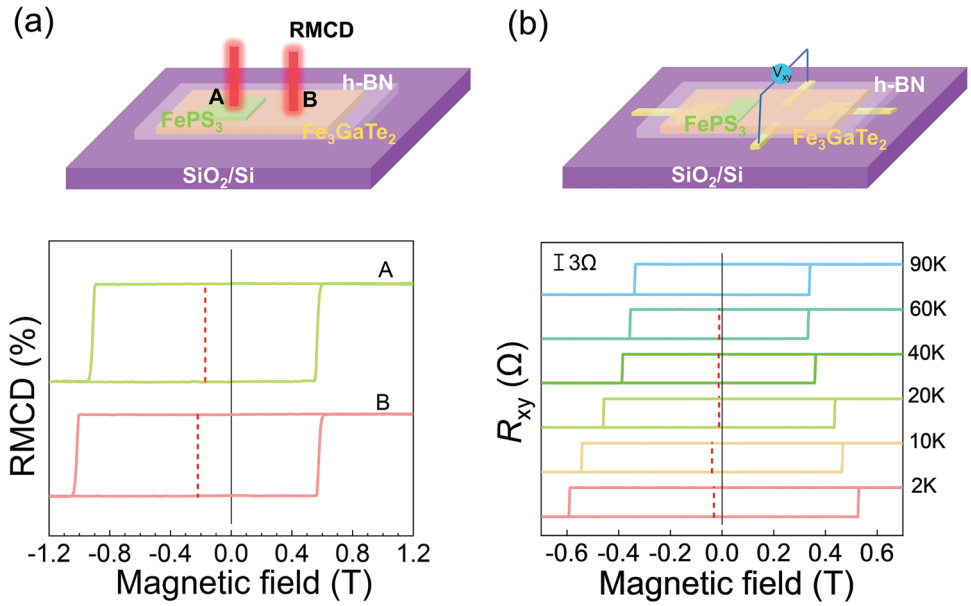

Figure 4. a) Schematic of the half-covered $FePS_3/Fe_3GaTe_2$ heterostructure measured by RMCD (upper panel). RMCD hysteresis loops of $FePS_3/Fe_3GaTe_2$ region (region A) and exposed Fe_3GaTe_2 region (region B) at 2 K (lower panel). b) Schematic of the half-covered $FePS_3/Fe_3GaTe_2$ device measured by AHE (upper panel). Temperature-dependent R_{xy} of exposed Fe_3GaTe_2 region under $H_{cool} = 0.5$ T, which is connected to the region of the same Fe_3GaTe_2 flake (15 nm) covered by $FePS_3$ (5 nm) in Device 2 (lower panel).

2.3. Non-Local EB Effect

Particularly, the non-local EB effect was observed in $FePS_3/Fe_3GaTe_2$ heterostructures. The $FePS_3/Fe_3GaTe_2$ heterostructures with varied interfacial configurations were constructed, where the interfacial configuration is adjusted by selectively exposing or covering part of the Fe_3GaTe_2 flakes, as illustrated in the upper panels of **Figures** 4a,b. As shown in Figure 4a, the RMCD was conducted on two separated regions (labeled A and B in Figure 4a) of the same Fe_3GaTe_2 flake, region A was directly covered by $FePS_3$ flake while region B was exposed. RMCD hysteresis loops of both A and B regions exhibit similar features, where the negative EB and a substantially large $|H_{EB}|$ even up to 200 mT at 2 K were observed. In addition, the temperature-dependent R_{xy} measured on a bare region of the Fe_3GaTe_2 flake (Device 2, the other region of the same Fe_3GaTe_2 flake was covered by $FePS_3$) also reveals the non-local EB effect. As shown in the lower panel of Figure 4b, a negative EB, a substantially large $|H_{EB}|$ up to 40 mT, and a T_b of ≈90 K were observed. The T_b and negative EB of Device 2 with Fe_3GaTe_2 partially covered by $FePS_3$ are consistent with those of Device 4 with Fe_3GaTe_2 having a similar thickness and fully covered by $FePS_3$ (Figure S8, Supporting Information). Such phenomena indicate that EB can effectively propagate in the transverse direction at the micrometer scale. Manipulating magnetization at lateral scales provides a promising way for constructing novel spin logic devices such as magnetoelectric spin-orbit logic (MESO).[43] The non-local EB effect is attributed to the itinerant ferromagnetic properties and the single magnetic domain of Fe_3GaTe_2 flakes.[11,44]

2.4. Physical Mechanism of Polarity-Reversal of EB

The observed polarity-reversal of EB as the temperature increases under a suitable high H_{cool} is intriguing and rarely reported in other vdW heterostructures. For $FePS_3/Fe_3GaTe_2$ heterostructure, $FePS_3$ possesses a higher work function (4.9 eV, insulating)[45] compared to Fe_3GaTe_2 (≈4.4 eV, metallic),[46,47] such that charge transfer from Fe_3GaTe_2 to $FePS_3$ occurs at the interface, as illustrated in the upper panel of **Figure** 5a. Electron doping causes the magnetic ground state of $FePS_3$ to transform from AFM order to ferrimagnetic (FIM) order, as demonstrated by the intercalation of organic cations in $FePS_3$.[48] In the FIM order of electron-doped $FePS_3$, the two ferromagnetic zigzag chains of Fe atoms possess unequal magnetic moments, producing net magnetic moments (ΔM), as shown in the lower panel of Figure 5a. The FIM-$FePS_3$ retains the large coercive field of $FePS_3$, which prevents ΔM from being fully aligned within the sweeping magnetic field range during EB measurements at low temperatures, such that an unusual temperature-dependent hysteresis loop of FIM-$FePS_3$ was observed.[48] As shown in Figure S9 (Supporting Information), as temperature increases to 60 K, the hysteresis loops become more pronounced, and ΔM gradually increases, which is ascribed to that thermal kinetic energy promotes the alignment of magnetic moments. Thermal fluctuations would weaken the exchange coupling as the temperature increases, therefore the trade-off between the magnitude of ΔM and thermal fluctuations lead to the maximum EB in a range of 40–60 K as the temperature increases.

The mechanisms of the negative EB under low H_{cool} and temperature-dependent polarity-reversal (from negative to

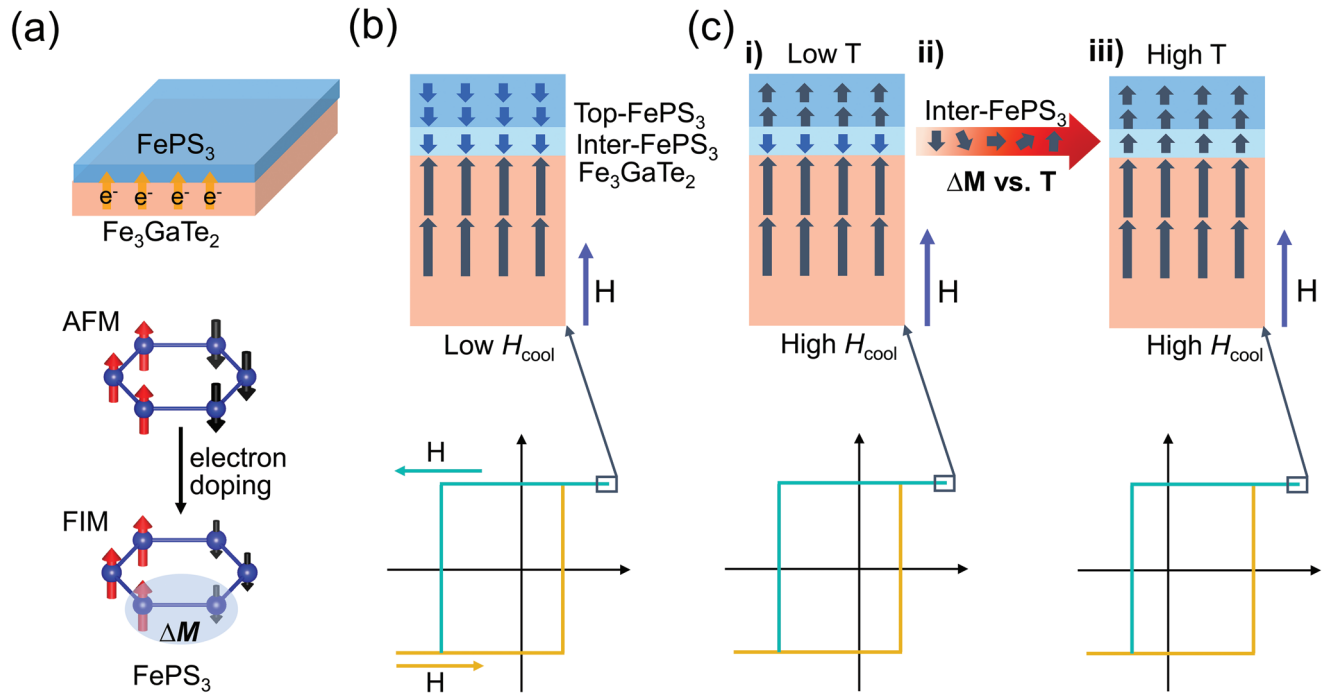

Figure 5. a) Upper panel: schematic of electron transfer from Fe_3GaTe_2 to $FePS_3$ at the interface. Lower panel: the zigzag AFM order of $FePS_3$ and the FIM order with ΔM of doped $FePS_3$, where arrows indicate the orientation and magnitude of the magnetic moments of Fe atoms. b,c) Upper panels: schematic of a model for the magnetic configurations of top-$FePS_3$/inter-$FePS_3$/Fe_3GaTe_2 under low H_{cool} b) and high H_{cool} c), respectively. Arrows indicate the orientation and magnitude of interfacial Fe_3GaTe_2 or ΔM of inter-$FePS_3$ and top-$FePS_3$. Lower panels: negative EB under low H_{cool}, negative EB under high H_{cool} at a low temperature c-i), and positive EB under high H_{cool} at a high temperature (c-iii), respectively. (c-ii) Schematic diagram showing the upward rotation of ΔM of the inter-$FePS_3$ as temperature increases.

positive) of EB under high H_{cool} were then discussed. If the interfacial exchange coupling is FM, a negative EB is always formed regardless of the field-cooling conditions. If the interfacial exchange coupling is AFM, the polarity of EB is dependent on the field-cooling conditions.[7,49] Therefore, the observation of positive EB under high H_{cool} in $FePS_3/Fe_3GaTe_2$ heterostructures indicates that their interfacial exchange coupling is AFM.

Moreover, the temperature-dependent polarity-reversal of EB cannot be explained by a simple AFM coupling interface, and a relatively complex model composed of multiple structures is necessary to understand such phenomena. As shown in Figure 5b, the $FePS_3/Fe_3GaTe_2$ heterostructure can be divided into three portions[19,50]: the bottom Fe_3GaTe_2 portion, the interfacial $FePS_3$ portion in direct contact with Fe_3GaTe_2 (inter-$FePS_3$), and the top $FePS_3$ portion (top-$FePS_3$). The magnetic configurations of the $FePS_3/Fe_3GaTe_2$ heterostructure are determined by the competition between the energy of the interfacial exchange coupling at the interfacial-$FePS_3/Fe_3GaTe_2$ interface (E_{ex}), the interlayer magnetic interaction between the top-$FePS_3$ and inter-$FePS_3$ portions of doped $FePS_3$ layer (E_{inter}), and the Zeeman energy for aligning the magnetic moments (E_Z).[8] Take the heterostructure being field-cooled along a positive direction as an example. The E_Z tends to make the magnetic moments of Fe_3GaTe_2 and the ΔM of both inter-$FePS_3$ and top-$FePS_3$ point to the direction of the external magnetic field (upward); the E_{ex} tends to make the ΔM of inter-$FePS_3$ point to a direction (downward) opposite to that of the magnetic moments of Fe_3GaTe_2 due to the interfacial AFM coupling; and the E_{inter} tends to make the ΔM of inter-$FePS_3$ and the ΔM of top-$FePS_3$ align in the same direction.

When H_{cool} is low, E_Z is substantially small, causing the ΔM of inter-$FePS_3$ to point downward driven by the E_{ex}, and the ΔM of top-$FePS_3$ to point downward driven by the E_{inter}, such that the corresponding magnetic configuration of the top-$FePS_3$/inter-$FePS_3/Fe_3GaTe_2$ is initially formed as ↓↓/↓↓/↑↑, as illustrated in the upper panel of Figure 5b. To overcome the AFM interfacial coupling, a larger magnitude of H_C^- H_C^- is required to reverse the magnetic moments of Fe_3GaTe_2 during the backward process, while a smaller magnitude of H_C^+ H_C^+ is needed during the forward process, and thus a negative EB is observed, as shown in the lower panel of Figure 5b.

When enhancing H_{cool} to a high level, E_Z increases, and the ΔM of top-$FePS_3$ points upward driven by the E_Z, while the direction of ΔM of the inter-$FePS_3$ is determined by the competition between E_{ex}, E_Z, and E_{inter}. At low temperatures, E_{ex} dominates the magnetic configuration of the inter-$FePS_3$ ($E_{ex} > E_Z + E_{inter}$), and thus the ΔM of inter-$FePS_3$ point downward, and the corresponding magnetic configuration of the top-$FePS_3$/inter-$FePS_3/Fe_3GaTe_2$ is initially formed as ↑↑/↓↓/↑↑, as illustrated in the upper panel of Figure 5c (i). Because the exchange interactions are short-range interactions, the magnetic configuration of inter-$FePS_3$ dominates the EB effect. In view of this, similar to the case of the heterostructure cooled with a low H_{cool}, a negative EB is observed, as shown in the lower panel of Figure 5c (i). As the temperature increases, thermal fluctuation increases and the E_{ex} decreases, the E_{ex} is no longer sufficient

enough to pin the ΔM of inter-$FePS_3$ pointing downward, and the ΔM of inter-$FePS_3$ gradually rotates upward driven by the E_Z and E_{inter}, as illustrated in Figure 5c (ii). Therefore, at a suitable high temperature, the ΔM of inter-$FePS_3$ points upward, and the corresponding magnetic configuration of the top-$FePS_3$/inter-$FePS_3$/Fe_3GaTe_2 is formed as ↑↑/↑↑/↑↑, as illustrated in the upper panel of Figure 5c (iii). Benefiting from AFM interfacial coupling, a smaller magnitude of H_C^- H_C^- is required to reverse the magnetic moments of Fe_3GaTe_2 during the backward process, while a larger magnitude of H_C^+ H_C^+ is needed during the forward process, and thus a positive H_{EB} shown in the lower panel of Figure 5c (iii) is observed. Micromagnetic simulations based on the proposed sandwich structure were also conducted to simulate the process of gradually rotating ΔM in the inter-$FePS_3$ layer as temperature increases under the competition between E_{inter} and E_{ex}, as shown in Figure S10 (Supporting Information). The results of micromagnetic simulations reveal the possible reversal of ΔM of the inter-$FePS_3$ as the temperature increases, which leads to the temperature-dependent polarity reversal of EB.

3. Conclusion

In summary, an obvious and considerable EB effect was observed in the $FePS_3$/Fe_3GaTe_2 heterostructure, and in particular, the EB effect exhibits non-local properties and temperature-dependent polarity-reversal behavior. Due to the itinerant ferromagnetism and single magnetic domain state of Fe_3GaTe_2, for the Fe_3GaTe_2 flake partially covered with $FePS_3$, the bare region exhibits similar EB characteristics as the covered region. The temperature-dependent polarity-reversal behavior of EB is cooling field dependent, where with increasing temperature, the negative EB reverses to the positive EB under suitable high cooling field conditions, while the negative polarity of EB remains unchanged under relatively low cooling field conditions. An intuitive model composed of top-$FePS_3$/inter-$FePS_3$/Fe_3GaTe_2 sandwich structure is proposed to understand the polarity-reversal behavior, where the charge transfer from Fe_3GaTe_2 to $FePS_3$ at the interface induces ΔM in $FePS_3$, and the orientations of ΔM of the interfacial $FePS_3$ layer, which is determined by the competition between E_{ex}, E_{inter} and E_Z, dominates the polarity of EB. The findings of this work provide new insights for understanding the EB effect in various vdW heterostructures and offer emerging strategies for constructing innovative spin logic devices.

4. Experimental Section

Device Fabrication: Fe_3GaTe_2 and $FePS_3$ bulk crystals were grown by the flux method. To minimize the oxidation and contamination, thin Fe_3GaTe_2 and $FePS_3$ flakes were obtained by mechanical exfoliation, and the heterostructures were prepared by dry transfer techniques with poly(dimethylsiloxane) (PDMS) stamps onto the pre-pattered electrodes in a glove box filled with Ar gas, where H_2O and O_2 levels were maintained below 0.1 ppm. Before performing characterization and measurements, the devices were encapsulated by h-BN.

Transport Measurements and RMCD Measurements: Electrical transport measurements were performed in a commercial physical property measurement system (PPMS, Quantum Design Dynacool-9) with lock-in techniques (SR830). The RMCD measurements were conducted using a standard lab-made RMCD setup and the wavelength of HeNe laser was 633 nm.

Characterization: Raman measurements were performed via an inVia confocal Raman microscope (Renishaw) with a 532 nm laser at room temperature. The laser power was kept below 0.05 mW to avoid local heating. Atomic force microscopy (AFM) images were carried out by a Benyuan system (CSPM5500). The thickness was determined by AFM and color contrast analysis based on optical images.

Supporting Information

Supporting Information is available from the Wiley Online Library or from the author.

Acknowledgements

H.X. and B.L. contributed equally to this work. This work was supported by the National Natural Science Foundation of China (Grant Nos. 92065206, 52372011, U22A20123, 12304042), the National Key R&D Program of China (Grant No. 2022YFA1602704), the Natural Science Foundation of Shandong Province (Grant Nos. ZR2023ZD10, ZR2022MF228), Guangdong Provincial Quantum Science Strategic Initiative (Grant No. GDZX2301008), Basic and Applied Basic Research Foundation of Guangdong Province (Grant Nos. 2023A1515110508), Postdoctoral Fellowship Program of CPSF (Grant No. GZC20231434), Postdoctoral Innovation Program of Shandong Province (Grant No. SDCX-ZG-202400329), the Open Project of Guangdong Provincial Key Laboratory of Magnetoelectric Physics and Devices (Grant No. 2022B1212010008), Open Project of Chinese Academy of Science Sharing Service Platform of CAS Large Research Infrastructures (Grant No. 2023SECUFPT001399), the Shanghai Science and Technology Innovation Action Plan (Grant No. 21JC1402000) and the Double First-Class Initiative Fund of ShanghaiTech University.

Conflict of Interest

The authors declare no conflict of interest.

Data Availability Statement

The data that support the findings of this study are available from the corresponding author upon reasonable request.

Keywords

exchange bias, non-local manipulation, polarity-reversal, van der Waals heterostructure

Received: August 6, 2024
Revised: October 16, 2024
Published online: November 4, 2024

[1] Y. Wu, S. Zhang, J. Zhang, W. Wang, Y. L. Zhu, J. Hu, G. Yin, K. Wong, C. Fang, C. Wan, X. Han, Q. Shao, T. Taniguchi, K. Watanabe, J. Zang, Z. Mao, X. Zhang, K. L. Wang, *Nat. Commun.* **2020**, *11*, 3860.
[2] Y. Wu, B. Francisco, Z. Chen, W. Wang, Y. Zhang, C. Wan, X. Han, H. Chi, Y. Hou, A. Lodesani, G. Yin, K. Liu, Y.-T. Cui, K. L. Wang, J. S. Moodera, *Adv. Mater.* **2022**, *34*, 2110583.
[3] K. Li, L. Wang, Y. Wang, Y. Guo, S. Lv, Y. He, W. Lin, T. Min, S. Hu, S. Yang, D. Xue, A. Zheng, S. Yang, X. Ding, *Adv. Mater.* **2024**, *36*, 2312137.

[4] I. A. Golovchanskiy, N. N. Abramov, V. S. Stolyarov, V. V. Bolginov, V. V. Ryazanov, A. A. Golubov, A. V. Ustinov, *Adv. Funct. Mater.* **2018**, *28*, 1802375.
[5] L. Pan, A. Grutter, P. Zhang, X. Che, T. Nozaki, A. Stern, M. Street, B. Zhang, B. Casas, Q. L. He, E. S. Choi, S. M. Disseler, D. A. Gilbert, G. Yin, Q. Shao, P. Deng, Y. Wu, X. Liu, X. Kou, S. Masashi, X. Han, C. Binek, S. Chambers, J. Xia, K. L. Wang, *Adv. Mater.* **2020**, *32*, 2001460.
[6] W. H. Meiklejohn, C. P. Bean, *Phys. Rev.* **1957**, *105*, 904.
[7] J. Nogués, I. K. Schuller, *J. Magn. Magn. Mater.* **1999**, *192*, 203.
[8] F. Wang, D. Xiao, W. Yuan, J. Jiang, Y.-F. Zhao, L. Zhang, Y. Yao, W. Liu, Z. Zhang, C. Liu, J. Shi, W. Han, M. H. W. Chan, N. Samarth, C.-Z. Chang, *Nano Lett.* **2019**, *19*, 2945.
[9] T. M. J. Cham, R. J. Dorrian, X. S. Zhang, A. H. Dismukes, D. G. Chica, A. F. May, X. Roy, D. A. Muller, D. C. Ralph, Y. K. Luo, *Adv. Mater.* **2024**, *36*, 2305739.
[10] S. Peng, D. Zhu, W. Li, H. Wu, A. J. Grutter, D. A. Gilbert, J. Lu, D. Xiong, W. Cai, P. Shafer, K. L. Wang, W. Zhao, *Nat. Electron.* **2020**, *3*, 757.
[11] X. Huang, L. Zhang, L. Tong, Z. Li, Z. Peng, R. Lin, W. Shi, K.-H. Xue, H. Dai, H. Cheng, D. de Camargo Branco, J. Xu, J. Han, G. J. Cheng, X. Miao, L. Ye, *Nat. Commun.* **2023**, *14*, 2190.
[12] H. Aboulfadl, F. Seifried, M. Stueber, F. Muecklich, *Mater. Lett.* **2019**, *236*, 92.
[13] Y. Liu, Y. Huang, X. Duan, *Nature.* **2019**, *567*, 323.
[14] K. S. Novoselov, A. K. Geim, S. V. Morozov, D.-e. Jiang, Y. Zhang, S. V. Dubonos, I. V. Grigorieva, A. A. Firsov, *Science.* **2004**, *306*, 666.
[15] C. Gong, L. Li, Z. Li, H. Ji, A. Stern, Y. Xia, T. Cao, W. Bao, C. Wang, Y. Wang, *Nature.* **2017**, *546*, 265.
[16] B. Huang, G. Clark, E. Navarro-Moratalla, D. R. Klein, R. Cheng, K. L. Seyler, D. Zhong, E. Schmidgall, M. A. McGuire, D. H. Cobden, *Nature.* **2017**, *546*, 270.
[17] R. Zhu, W. Zhang, W. Shen, P. K. J. Wong, Q. Wang, Q. Liang, Z. Tian, Y. Zhai, C.-w. Qiu, A. T. S. Wee, *Nano Lett.* **2020**, *20*, 5030.
[18] H. Dai, H. Cheng, M. Cai, Q. Hao, Y. Xing, H. Chen, X. Chen, X. Wang, J.-B. Han, *ACS Appl. Mater. Interfaces.* **2021**, *13*, 24314.
[19] G. Hu, Y. Zhu, J. Xiang, T.-Y. Yang, M. Huang, Z. Wang, Z. Wang, P. Liu, Y. Zhang, C. Feng, D. Hou, W. Zhu, M. Gu, C.-H. Hsu, F.-C. Chuang, Y. Lu, B. Xiang, Y.-L. Chueh, *ACS Nano.* **2020**, *14*, 12037.
[20] K. Gu, X. Zhang, X. Liu, X. Guo, Z. Wu, S. Wang, Q. Song, W. Wang, L. Wei, P. Liu, J. Ma, Y. Xu, W. Niu, Y. Pu, *Adv. Sci.* **2024**, *11*, 2307034.
[21] T. Zhang, Y. Zhang, M. Huang, B. Li, Y. Sun, Z. Qu, X. Duan, C. Jiang, S. Yang, *Adv. Sci.* **2022**, *9*, 2105483.
[22] S. Albarakati, W.-Q. Xie, C. Tan, G. Zheng, M. Algarni, J. Li, J. Partridge, M. J. S. Spencer, L. Farrar, Y. Xiong, M. Tian, X. Wang, Y.-J. Zhao, L. Wang, *Nano Lett.* **2022**, *22*, 6166.
[23] Z. Ying, B. Chen, C. Li, B. Wei, Z. Dai, F. Guo, D. Pan, H. Zhang, D. Wu, X. Wang, S. Zhang, F. Fei, F. Song, *Nano Lett.* **2023**, *23*, 765.
[24] L. Zhang, X. Huang, H. Dai, M. Wang, H. Cheng, L. Tong, Z. Li, X. Han, X. Wang, L. Ye, J. Han, *Adv. Mater.* **2020**, *32*, 2002032.
[25] Y. Wu, W. Wang, L. Pan, K. L. Wang, *Adv. Mater.* **2022**, *34*, 2105266.
[26] A. van den Brink, G. Vermijs, A. Solignac, J. Koo, J. T. Kohlhepp, H. J. M. Swagten, B. Koopmans, *Nat. Commun.* **2016**, *7*, 10854.
[27] Y.-W. Oh, S.-h. C. Baek, Y. Kim, H. Y. Lee, K.-D. Lee, C.-G. Yang, E.-S. Park, K.-S. Lee, K.-W. Kim, G. Go, *Nat. Nanotechnol.* **2016**, *11*, 878.
[28] Deepak, A. K., S. M. Yusuf, *Phys. Rev. Mater.* **2021**, *5*, 124402.
[29] F. Hong, Z. Cheng, J. Wang, X. Wang, S. Dou, *Appl. Phys. Lett.* **2012**, *101*, 121913.
[30] G. Zhang, F. Guo, H. Wu, X. Wen, L. Yang, W. Jin, W. Zhang, H. Chang, *Nat. Commun.* **2022**, *13*, 5067.
[31] M. Wang, B. Lei, K. Zhu, Y. Deng, M. Tian, Z. Xiang, T. Wu, X. Chen, *npj 2D Mater. Appl.* **2024**, *8*, 22.
[32] W. Jin, G. Zhang, H. Wu, L. Yang, W. Zhang, H. Chang, *ACS Appl. Mater. Interfaces.* **2023**, *15*, 36519.
[33] W. Li, W. Zhu, G. Zhang, H. Wu, S. Zhu, R. Li, E. Zhang, X. Zhang, Y. Deng, J. Zhang, L. Zhao, H. Chang, K. Wang, *Adv. Mater.* **2023**, *35*, 2303688.
[34] S. N. Kajale, T. Nguyen, C. A. Chao, D. C. Bono, A. Boonkird, M. Li, D. Sarkar, *Nat. Commun.* **2024**, *15*, 1485.
[35] A. R. Wildes, D. Lançon, M. K. Chan, F. Weickert, N. Harrison, V. Simonet, M. E. Zhitomirsky, M. V. Gvozdikova, T. Ziman, H. M. Rønnow, *Phys. Rev. B.* **2020**, *101*, 024415.
[36] J.-U. Lee, S. Lee, J. H. Ryoo, S. Kang, T. Y. Kim, P. Kim, C.-H. Park, J.-G. Park, H. Cheong, *Nano Lett.* **2016**, *16*, 7433.
[37] Z. Cheng, T. A. Shifa, F. Wang, Y. Gao, P. He, K. Zhang, C. Jiang, Q. Liu, J. He, *Adv. Mater.* **2018**, *30*, 1707433.
[38] A. Bhutani, J. L. Zuo, R. D. McAuliffe, C. R. dela Cruz, D. P. Shoemaker, *Phys. Rev. Mater.* **2020**, *4*, 034411.
[39] A. P. Malozemoff, *Phys. Rev. B.* **1987**, *35*, 3679.
[40] H. K. Gweon, S. Y. Lee, H. Y. Kwon, J. Jeong, H. J. Chang, K.-W. Kim, Z. Q. Qiu, H. Ryu, C. Jang, J. W. Choi, *Nano Lett.* **2021**, *21*, 1672.
[41] Z. Ye, A. Balkanci, A. Martini, M. Z. Baykara, *Phys. Rev. B.* **2017**, *96*, 115401.
[42] J. C. Spear, J. P. Custer, J. D. Batteas, *Nanoscale.* **2015**, *7*, 10021.
[43] S. Manipatruni, D. E. Nikonov, C.-C. Lin, T. A. Gosavi, H. Liu, B. Prasad, Y.-L. Huang, E. Bonturim, R. Ramesh, I. A. Young, *Nature.* **2019**, *565*, 35.
[44] H. Dai, M. Cai, Q. Hao, Q. Liu, Y. Xing, H. Chen, X. Chen, X. Wang, H.-H. Fu, J. Han, *ACS Nano.* **2022**, *16*, 12437.
[45] M. Ramos, M. Gadea, S. Mañas-Valero, C. Boix-Constant, E. Henríquez-Guerra, M. A. Díaz-García, E. Coronado, M. R. Calvo, *Nanoscale Adv.* **2024**, *6*, 1909.
[46] E. Ko, *Sci. Rep.* **2022**, *12*, 5101.
[47] Y. Zhang, X. Li, J. Sheng, S. Yu, J. Zhang, Y. Su, *Appl. Phys. Lett.* **2023**, *123*, 192402.
[48] M.-J. Mi, L.-X. Yu, H. Xiao, B.-B. Lü, Y.-L. Wang, *Acta. Phys. Sin.* **2024**, *73*, 057501.
[49] J. Nogués, D. Lederman, T. Moran, I. K. Schuller, *Phys. Rev. Lett.* **1996**, *76*, 4624.
[50] W. Qi, F. Fei, Z. Zhang, B. Chen, H. Xie, B. Wei, S. Zhang, F. Song, *Appl. Phys. Lett.* **2024**, *125*, 023101.